Variable radio-frequency cold atmospheric He + O_2 discharges: from electron-heating mechanism to reactive species delivery

Variable radio-frequency cold atmospheric He + O₂ discharges: from electron-heating mechanism to reactive species delivery

Aijun Yang[1]**, Mingzhe Rong**[1]**, Xiaohua Wang**[1]**, Dingxin Liu**[1,3] **and Michael G Kong**[1,2,3]

[1] State Key Laboratory of Electrical Insulation and Power Equipment, Xi'an Jiaotong University, 710049, People's Republic of China
[2] Frank Reidy Center for Bioelectrics, Department of Electrical and Computer Engineering, Old Dominion University, VA 23508, USA

E-mail: liudingxin@mail.xjtu.edu.cn and mkong@odu.edu

Abstract

Evolution of electron-heating processes with driving frequency and their effects on production reactive oxygen species (ROS) are studied for low-temperature radio-frequency atmospheric helium–oxygen plasma. With increasing frequency from 13.54 to 108.48 MHz at a constant power density of $40\,\mathrm{W\,cm^{-3}}$, the space-averaged electron density is found to increase by 35% but this is accompanied by marked decrease in the sheath thickness, the maximum electron temperature, and the electric field in the sheath by 76%, 46% and four-folds, respectively. As a result, plasma species generated via reactions with low threshold electron energy (e.g. O_2^*) experience more abundant production and those generated by energetic electrons (e.g. O and O^*) undergo a reduction in their number densities as the driving frequency increases. These frequency dependences directly regulate power dissipation in species produced directly by electrons, ROS concentrations, and ultimately plasma chemistry. Delivery of ROS is shown to be effective only from a boundary layer immediately above a sample surface, due to severely compromised diffusion and drift at atmospheric pressure, introducing a further frequency-dependent factor. In general, the increase of the driving frequency affects energetic and low-energy electrons differently and the contrast in frequency effects of different ROS is desirable for manipulating plasma chemistry as experienced by the sample.

(Some figures may appear in colour only in the online journal)

1. Introduction

Low-temperature atmospheric-pressure plasmas have in recent years attracted a great deal of attention due to their considerable promise as a basic technology platform for tackling some of our major societal challenges including environmental contamination [1–3], depletion of natural energy sources [5, 6], and healthcare provision [7, 8]. It is generally accepted that reactive oxygen species (ROS) and/or reactive nitrogen species

(RNS) generated in the electrical discharges are critical in enabling technology solutions to these challenges. In the search for application efficacy and efficiency, the driving frequency is usually varied in practice, as an obvious control parameter, over a wide spectrum from direct current to microwave [9–14]. Clearly, the selection of an optimal driving frequency is firstly influenced by technology readiness and economic considerations, for example the availability of suitable power source technologies with high output voltages at different frequencies and their costs for the intended applications. Importantly, the driving frequency strongly

---

[3] Authors to whom any correspondence should be addressed.

affects how the electrical power is coupled into the plasma and indeed how the coupled power is differentially dissipated onto electrons and heavy particles. The importance of this was already observed some 70 years ago with a dielectric-barrier discharge (DBD) in air of which ozone yield was found to be greater at higher driving frequencies but would suffer a drastic reduction by high gas temperature, a common by-product of high frequency operation [15]. The former of the two observations implies large electron density or large electron energy, whilst the latter suggests significant gas heating. However little has been reported in open literature of direct impact on electron temperature and electron density in high-pressure non-equilibrium plasmas by the driving frequency.

The advent of atmospheric-pressure glow discharges near room temperature makes it possible for direct plasma treatment of delicate materials such as living plant and human tissues without undue damage [16–19]. These and other emerging plasma applications require better and more quantitative understanding of how plasma ROS/RNS are produced with what density profiles and dynamics. In turn, this demands that the effects of the driving frequency are linked to electron generation and heating so that the driving frequency could be adjusted to promote specific plasma characteristics with few unwanted features (e.g. excessive gas heating). In this regard, there has been important progress in our understanding. For example, an increase in the driving frequency is found to decrease the gas breakdown voltage of radio-frequency (RF) atmospheric-pressure helium plasmas in the 1–30 MHz range [20] but further increase to 300 MHz may start to raise the breakdown voltage [21]. These have been attributed to, respectively, the availability of more seed electrons confined in the electrode gap by the oscillating RF field [20] and the shrinking sheath at high frequencies that deprives electrons of adequate space for acceleration [21]. High driving frequencies are also found to broaden the range of stable operation for RF atmospheric-pressure helium plasmas by shifting the $\alpha-\gamma$ mode transition point to a higher discharge current [22–24]. At the lower frequency range of 1–100 kHz where DBDs are usually operated, it is found that the driving frequency can influence the supply of electrons involved in the initiation and sustainment of the discharge. A high driving frequency can suppress multiple discharge events during one half voltage cycle in DBDs [25], but a too high frequency may prevent electrons from reaching the dielectric layers of the electrodes and from setting up an adequate memory voltage for controlling the discharge current [26]. Above the RF range, microwave microplasmas are found to be more intense with increasing driving frequency [27].

These studies highlight that the driving frequency could possibly be used to regulate electron production and electron-heating processes with a simultaneous effect on the heating of the plasma-forming gas and heavy particles including ions. Energy dissipation to ions is undesirable since ionic reactions in general contribute little to the formation of most ROS/RNS as shown in the case of ozone [28]. It is therefore of great interest to understand how the dissipated electrical power is shared out between electrons and ions at different driving frequencies and indeed how such energy

partition may influence ROS/RNS production; a central issue of how appropriate plasma physics is translated into application efficacy and efficiency. Some extrapolation of how the driving frequency affects electron heating may be made from literature [20–29], but only indirectly so far, as most reported results were obtained without an important constraint of constant power density though there are few exceptions [29]. Furthermore, most published studies employ an inert feedstock gas to focus on ionization and electron-heating processes. Consequently, little is known of how the driving frequency may affect electron-heating processes in the presence of a molecular gas (e.g. O_2 and N_2) and also the formation of ROS/RNS. This is a critical knowledge gap that would help translate the current basic understanding of plasma physics into technology solutions to application requirements. This is the main motivation for the present work.

When a molecular gas such as oxygen is mixed into a noble gas for plasma generation, the physics and chemistry of low-temperature atmospheric-pressure plasmas undergo significant change. There have been extensive studies of low-temperature atmospheric-pressure plasmas in He + O_2 mixture [30–34], yet the role of the driving frequency in electron and ion heating as well as in the formation of reactive plasma species is largely uncharted. Given the current lack of suitable diagnostic tools for detailed dynamics of electrons and ions, we have recourse to a computational approach with a one-dimensional fluid model [35] whose results are found to agree with experimental observations [13, 24] and also predictions of similar fluid models [34, 36, 37]. For this study, we consider an RF atmospheric-pressure He–O_2 plasma sustained between two parallel-plate electrodes from a base frequency of $f_0 = 13.56$ MHz up to 108.48 MHz ($=8 f_0$) as there is a good understanding of electron kinetics and sheath dynamics, both critically linked to electron and ion heating, in RF atmospheric helium plasmas [38, 39]. It is expected that the conclusions reached from this investigation should be qualitatively applicable to other atmospheric plasmas including atmospheric DBDs and higher frequency plasmas.

With the fluid model and its reaction chemistry model described in section 2, electron-heating characteristics are presented and their dependence on the driving frequency discussed in section 3. Frequency effects on electron production are linked to the dissipated power, its coupling to electrons and ions, and the relative importance of elastic and inelastic collisions of electrons in section 4. These electron-heating properties are then used to discuss ROS production and utilization, in terms of the concentrations of ROS in the plasma bulk (section 5) and their wall fluxes to the electrodes used here as an indicator of what a sample may experience (section 6). Finally a summary of the conclusions drawn is provided in section 7.

2. Description of the computational model

The electrode configuration considered here consists of two parallel-plate electrodes with a narrow electrode gap of 2 mm and a large electrode width; similar to those used in experimental studies [24]. A large length-gap aspect

ratio is useful for achieving stable homogenous plasmas experimentally and also for enabling a one-dimensional computational treatment. The plasma-sustaining voltage has a sinusoidal waveform with a total dissipated power density of 40 W cm^{-3} and at a variable driving frequency, f, from 13.56 to 108.48 MHz. The figure of 40 W cm^{-3} is not experimentally uncommon for RF plasmas in atmospheric helium, and for this simulation study it is obtained from integrating the product of the applied voltage and the current density. The feedstock gas is a He + O$_2$ mixture at atmospheric pressure, with the O$_2$ admixture at 0.5% established from the condition for the most abundant production of oxygen atoms [34], a key plasma ROS with large oxidation potential, and also from that for the most effective plasma denaturation of proteins [40] and plasma inactivation of bacterial spores [41]. The gas temperature is held at 350 K, which may be achieved with the electrode temperature held constant with circulating cooling water.

A one-dimensional fluid model is used with its details previously reported [35, 42]. Similar to other fluid models [36–38], the drift–diffusion approximation is employed to estimate the mean electron velocity by neglecting electron and ion inertia. Its justification is based on the fact that the collision frequency is much higher than the driving frequency of the plasma at atmospheric pressure and the mean-free path length is small compared to the Debye length [39]. This was supported by comparing results of the drift–diffusion equation with those of kinetic simulation for RF microplasmas [38, 39] whose electric field is higher than that in the present study, and the comparison supports the use of the drift–diffusion equation. The electron energy distribution function (EEDF) is obtained by solving the Boltzmann equation with BOLSIG+.

The fluid model requires simultaneous solution to the drift–diffusion equation for each species, the electron energy equation and Poisson's equation. The model incorporates 17 plasma species and 60 reactions among them [35, 42], selected from a global model [33]. Specifically, the 17 plasma species include the ground-state oxygen atoms (O), excited-state oxygen atoms (O*), excited oxygen molecules O$_2^*$ (including O$_2(a\ ^1\Delta_g)$ and O$_2(b\ ^1\Sigma_g^+)$), ozone (O$_3$), super oxide (O$_2^-$), all known to be important in biology [43], environmental science [2], and surface engineering [9, 44], as well as positive ions (O$_2^+$ and O$_4^+$) and negative ions (O$^-$, O$_2^-$ and O$_3^-$). The 60 reactions mainly include the momentum transfer and inelastic collisions of electrons with He and O$_2$ (e.g. ionization, dissociation, dissociative excitation, dissociative attachment), the Penning ionization by helium metastables, the ion–neutral reactions, the collisional relaxation of excited species, the recombination of ionic species, and other reactions among neutral species. Boundary conditions used in this study are identical to those used previously [35, 42], and are consistent with those used in similar fluid models of atmospheric-pressure plasmas [36, 37]. It should be noted that a Boltzmann Solver, BOLSIG+, is used to calculate the EEDF and the corresponding reaction rate coefficients [45]. For spatial distribution of the electron density and the electron energy, the sheath boundary is determined using $n_e = 0.3(n_c - n_a)$, in which n_c and n_a are the densities of cations and anions, respectively, for electronegative gases. This is derived with a modification to a similar treatment of the sheath boundary for electropositive gases [29].
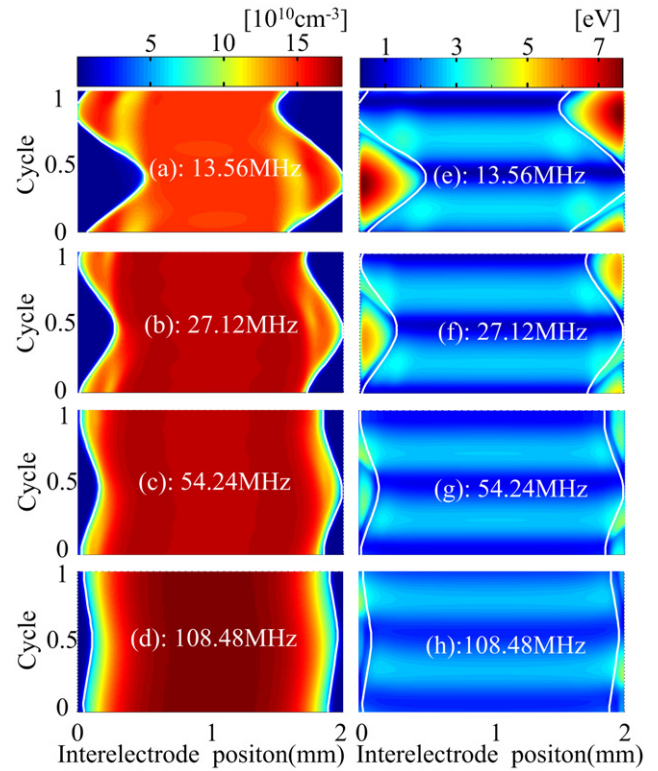

Figure 1. Spatio-temporal evolution of the electron density (*a*)–(*d*) and the electron temperature (*e*)–(*h*) at different driving frequencies. The white lines indicate the sheath edges.

3. Electron-heating mechanisms

Driving frequency effects on electron density and electron energy of RF atmospheric-pressure plasmas have been studied for inert gases (e.g. He, Ar) [22–29]. For example, the increase of the driving frequency is known to generally reduce the gas breakdown voltage in RF atmospheric-pressure helium discharges due to an increase in available seed electrons [20, 21]. Electrons underpin production of all other plasma species, so factors that affect electron production and loss are likely to have a large impact on ROS production and the overall chemical composition of the ionized gas. With electronegative gases such as O$_2$, electron attachment as an electron loss route becomes important and it becomes necessary to examine whether this may affect the electron and ion heating as well as the chemical composition of ROS. In this section, we consider electron density and electron temperature and with their characteristics investigate the main electron-heating mechanisms as the driving frequency is varied.

Figure 1 shows the spatio-temporal evolution of the electron density (n_e) and the electron temperature (T_e) at four driving frequencies (i.e. $f = f_0$, $2f_0$, $4f_0$ and $8f_0$). It can be seen that the quasi-neutral region (i.e. the plasma bulk with abundant electrons) oscillates between the two electrodes, similar to the observations in atmospheric helium discharges [38, 39] but now with larger sheath thickness d_s. The sheath thickness is found to reduce monotonically with $d_s = 527\,\mu$m, 308\,μm, 181\,μm and 124\,μm for 13.56 MHz, 27.12 MHz, 54.24 MHz and 108.48 MHz, respectively. This means a decrease in the sheath thickness by a factor of
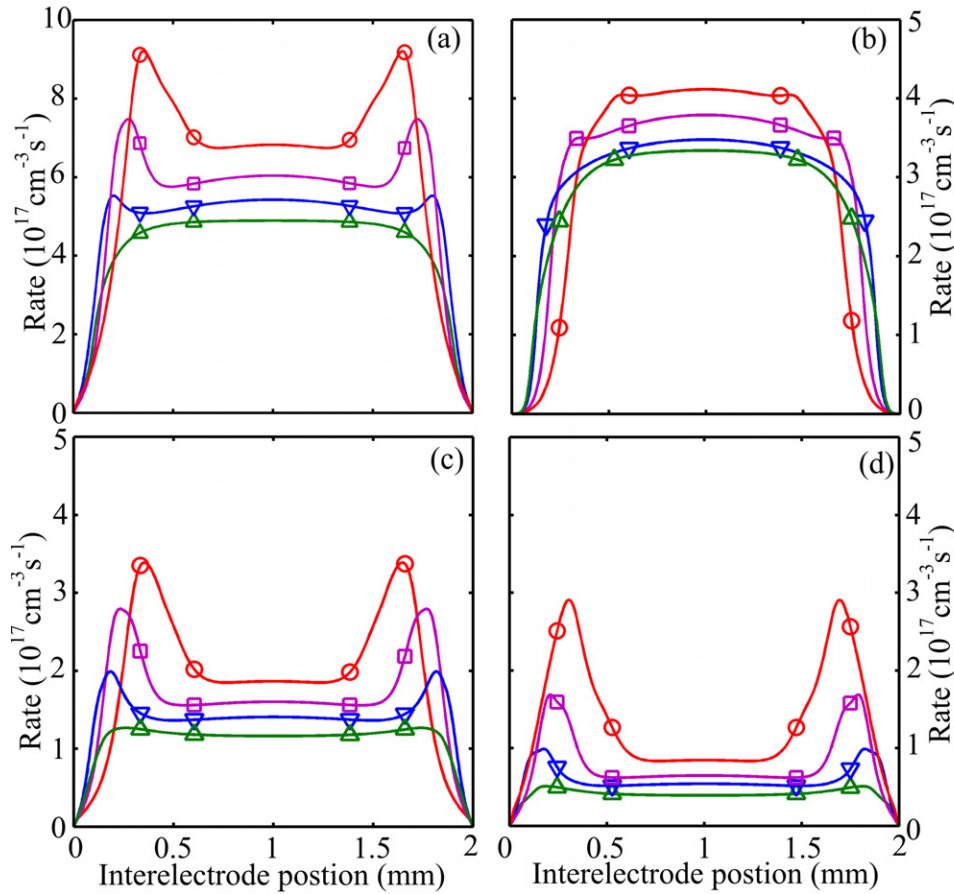
Figure 2. Spatial profiles of phase-averaged electron generation rates: (*a*) the total; (*b*) electron detachment; (*c*) electron-impact ionization; (*d*) Penning ionization by He metastables at 13.56 MHz (–○–), 27.12 MHz (–□–), 54.24 MHz (–▽–), and 108.48 MHz (–△–).

527 μm/124 μm $=$ 4.25 with an eight-fold increase in the driving frequency for the He + O$_2$ plasma. As the sheath thickness is essentially the distance over which electrons can be efficiently accelerated for initiating an avalanche, the reversal proportional dependence of d_s on f observed in figure 1 suggests a more effective initiation of avalanche at high frequencies. Furthermore, the increase of the driving frequency from 13.56 to 108.48 MHz is found to reduce the peak applied voltage from 511 to 340 V.

The above observations may be understood from the fact that with a large driving frequency the electrons have less time to drift to the instantaneous anode and are more likely to be trapped between the two electrodes [46]. Strong electron trapping leads to both a reduced electron loss to the electrodes and an availability of more seed electrons for subsequent ionization. These two factors combine to lower the minimum necessary electron density in the sheath region for the avalanche, and as such lower the necessary sheath thickness for adequate electron acceleration. In addition, the availability of more seed electrons in the electrode gap reduces the plasma-sustaining voltage. Similar trends have been observed both in experiments and simulation for RF atmospheric helium plasmas [24, 29].

It is evident in figure 1 that the electron density increases only slightly with the driving frequency with the maximum electron density being 1.58 cm^{-3}, 1.70 cm^{-3}, 1.71 cm^{-3}, and

1.81×10^{10} cm^{-3} for 13.56 MHz, 27.12 MHz, 54.24 MHz and 108.48 MHz, respectively. In other words, the maximum electron density increases by $\sim$15% over an eight-fold increase in the driving frequency. For the eight-fold frequency increase, the space-averaged electron density is found to increase by a larger margin of 36% due to the more sensitive frequency dependence of the sheath thickness (figure 1(*a*)). A modest dependence of the electron density on the driving frequency was in fact observed experimentally in an RF atmospheric-pressure helium-air plasma for which the electron density was found to increase by about 25% when the frequency was increased from 10 to 80 MHz, also eight-fold [47]. This modest increase in the electron density is attributed to a reduction in the electron wall loss to the electrode since the electron generation rate reduces with frequency (see figure 2 and discussion therein). Reduced electron wall loss is evident in figures 1(*a*)–(*d*) where the plasma bulk boundary is seen to touch the electrode for $f \leqslant 27.12$ MHz but is prevented from reaching the electrodes at higher frequencies.

For the electron temperature on the other hand, it decreases sharply with the increase of the driving frequency in the sheath, but changes much less in the plasma bulk (see figures 1(*e*)–(*h*). The maximum electron temperature, $T_{e,max}$, is reached near the boundary of the sheath region, and is 7.71 eV, 5.63 eV, 4.17 eV, 4.16 eV (i.e. a drop of 54% from 7.71 eV) for 13.56 MHz, 27.12 MHz, 54.24 MHz and 108.48 MHz, respectively. Again

this is a result of the availability of more seed electrons at higher driving frequencies—the more abundant seed electrons from a discharge event allow for the next discharge event to be triggered with a smaller mean electron density. This phenomenon was observed experimentally also for RF atmospheric-pressure helium plasmas [47]. In the plasma bulk, the electron temperature is seen in figure 1(*b*) to reach 3.5–3.75 eV at 13.56 and 27.12 MHz but less than 3 eV at 54.24 MHz and above. In the sheath region on the other hand, the maximum electron temperature reduces to 3.5–3.75 eV for 54.24 MHz and above. This suggests that generation of plasma species in the plasma bulk is likely to be increasingly compromised with increasing frequency particularly for those with threshold energy much greater than 4 eV.

To understand the driving frequency effects on electron heating, figure 2 shows spatial profiles of phase-averaged rates of three main electron generation mechanisms at four different driving frequencies. Contrary to the trend of the electron density, the total generation rate (see figure 2(*a*)) decreases with the increase of the driving frequency. The reduction of the total electron generation rate at 108.48 MHz from its value at 13.56 MHz is 47% near the sheath edge and 28% in the plasma bulk (figure 2(*a*)), both greater than the 15% increase in the maximum electron density (figures 1(*a*)–(*d*). This may be understood from the dependence of electron generation rates on the electron temperature and the latter's dependence on the driving frequency. The main processes for electron production are the electron detachment, electron-impact ionization and Penning ionization by helium metastables, and their rates are plotted in figures 2(*b*)–(*d*). The rates of the two ionization processes have a bimodal shape, indicating their strong dependence on the electron temperature that is the largest near the sheath boundary. Penning ionization is directly influenced by helium metastables, and the latter are generated through $(e+He \rightarrow e+He^*)$ with a threshold electron energy of 19.8 eV. The threshold energy of the electron-impact ionization $(e + O_2 \rightarrow O_2^+ + 2e)$ is also high at 12.1 eV. So the electron-impact ionization and Penning ionization are sensitive to the electron temperature, particularly in the sheath region where the mean electron energy is likely to reach the ionization threshold energies. As the driving frequency increases, the mean electron temperature decreases sharply (figures 1(*e*)–(*h*)) and, as such, the electron-impact and Penning ionization rates also decrease sharply, again pronounced in the bimodal region.

For electron detachment on the other hand, the anions are mainly produced by dissociative attachment of $e + O_2 \rightarrow O^- + O(4.12 \text{ eV})$ and $e + O_3 \rightarrow O^- + O_2(3.54 \text{ eV})$. Compared to the ionization processes, the threshold energies for anion generation are much lower, hence their rates are less sensitive to the drastic reduction in T_e from 7.71 to 4.16 eV. This explains the slower decrease of the electron generation rate in figure 2(*b*) than in figures 2(*c*) and (*d*). As the electron detachment rates decrease with frequency, they are still affected more by the electron temperature than the electron density despite of their lower energy thresholds and less sensitive reliance on the electron temperature.

Frequency dependence of the mean electron energy changes the partition of the contributions of the three main electron generation mechanisms. The large threshold energy of the two ionization processes makes them more exposed to the reversal frequency dependence of the electron energy. Indeed, as the driving frequency rises from 13.56 MHz to 108.48 MHz, the contribution of electron detachment to the overall space-averaged electron production rate increases from 47% to 64%, whereas the contribution of the two ionization processes decreases from 31% and 22% to 26% and 10%, respectively. This highlights the dominant role of electron detachment in electron generation and the increase in its dominance with increasing frequency. It is interesting to note that the electronegativity of the He + O₂ plasma is higher than 1 even though there is only 0.5% of O₂ in the feedstock gas. Here, the electronegativity (α) is defined as the ratio of anion density (n_a) to the electron density (n_e), i.e. $\alpha = n_a/n_e$. Again this confirms that the electron detachment dominates electron production. This is also predicted by global modelling RF atmospheric He + O₂ plasma [33].

4. Power dissipation

For low-pressure plasmas, it is reasonable to assume that all power dissipated in the discharge is absorbed by electrons [48]. However at atmospheric pressure, ions can absorb significant energy from the electric field [49]. From the standpoint of plasma chemistry and applications relying on ROS/RNS, a large dissipated power density in electrons is desirable for the production of reactive plasma species. To see how the power dissipation into electrons and ions may vary with frequency at a constant total dissipated power (40 W cm⁻³), figure 3 show the spatial distributions of phase-averaged electron- and ion-coupling power densities for different driving frequencies. It is seen that the ion-coupling power density (P_i) can be large in the sheath region for $f < 27.12$ MHz. With increasing frequency, the above discussions in section 3 show a reducing sheath electric field (linked to reducing electron temperature) and a shrinking sheath region. This suggests that the ion acceleration is also likely to be compromised with increasing frequency, thus explaining the drastic reduction of the ion-coupling power in the sheath (figure 3(*b*)). Above 27.12 MHz, the power density coupled to ions is much smaller at some 6% of the total dissipated power. Hence a vast majority of the dissipated power is coupled to electrons above 27.12 MHz. As the sheath region becomes narrower with increasing frequency, it is not surprising that the spatial profile of the electron-coupling power density (P_e) broadens with increasing frequency. As a reference point, it is worth noting that the maximum ion–neutral collision and ion–electron collision frequencies are related to O_2^+ at $6 \times 10^5 \text{ s}^{-1}$ and $1 \times 10^4 \text{ s}^{-1}$, respectively.

The partition of the dissipated power density between electrons and ions may be seen more clearly with an analytical formulation of the partition of the dissipated power between electrons and ions. As the free path length is much smaller than the discharge gap, the ratio of P_e to P_i ($\eta = P_e/P_i$) can be estimated by
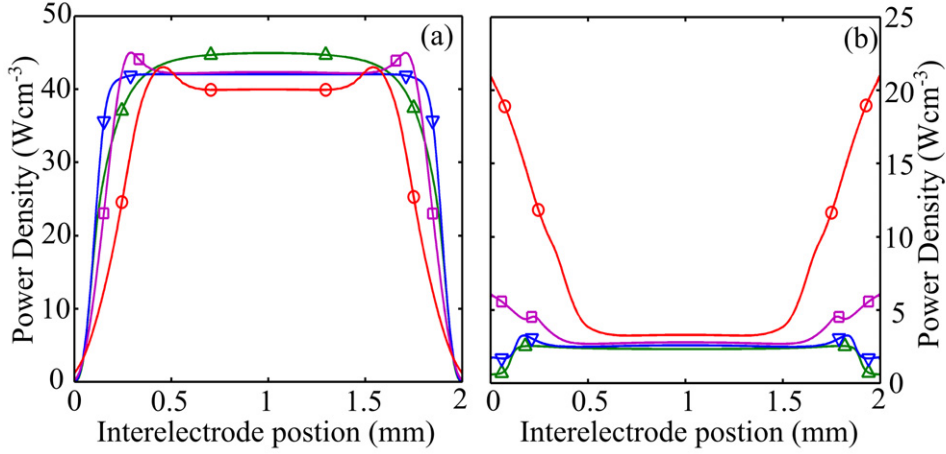
$$\eta = \frac{\mu_e n_e}{\sum_k \mu_{i,k} n_{i,k}}, \tag{1}$$

Figure 3. Spatial dependence of the dissipated power density into (*a*) electrons and (*b*) ions at 13.56 MHz (–○–), 27.12 MHz (–□–), 54.24 MHz (–▽–), and 108.48 MHz (–△–).

where μ_e is electron mobility, $\mu_{i,k}$ and $n_{i,k}$ are the mobility and density for *k*th ionic species, respectively. In the quasi-neutral bulk region, it can be simplified to

$$\eta_B = \frac{\mu_e}{\mu_i(2\alpha + 1)}, \qquad (2)$$

where μ_i is the weight-averaged ion mobility. In this study, the electronegativity α is found to decrease from 1.64 to 1.01 with the driving frequency increasing from 13.56 to 108.48 MHz. Using $\mu_e = 1100\,\mathrm{cm^2\,V^{-1}\,s^{-1}}$ and $\mu_i = 20\,\mathrm{cm^2\,V^{-1}\,s^{-1}}$ based on our previous study [33], it is found that $\eta_B = 12.8$–18.3 with larger values achieved at higher frequencies. In the sheath region, the relationship between the electron density and the ion density is difficult to estimate. However, when the driving frequency is above 27.12 MHz, the sheath width is much smaller than the bulk, and the ion-coupling power density in the sheath is close to that in the bulk (see figures 3(*b*)). So for $f \geqslant 27.12$ MHz, the majority of the input power is dissipated in the bulk region so approximating η as

$$\eta = \eta_B. \qquad (3)$$

Also, the space- and time-averaged $\bar{P}_e$ can be estimated as

$$\bar{P}_e = \bar{P}_{\mathrm{tot}}\frac{\eta}{\eta+1} = \bar{P}_{\mathrm{tot}}\frac{\mu_e}{\mu_e + \mu_i(2\alpha+1)}, \qquad (4)$$

where $\bar{P}_{\mathrm{tot}} = 40\,\mathrm{W\,cm^{-3}}$ is the spatio-temporal averaged input power density. Figure 3(*a*) shows that is $\bar{P}_{\mathrm{tot}}$ is $32.3\,\mathrm{W\,cm^{-3}}$, $36.6\,\mathrm{W\,cm^{-3}}$, $37.5\,\mathrm{W\,cm^{-3}}$ and $37.8\,\mathrm{W\,cm^{-3}}$ for $f = 13.56$ MHz, 27.12 MHz, 54.24 MHz and 108.48 MHz, respectively. And according to formula (4), it is $37.6\,\mathrm{W\,cm^{-3}}$, $37.7\,\mathrm{W\,cm^{-3}}$ and $37.9\,\mathrm{W\,cm^{-3}}$ for $f = 27.12$ MHz, 54.24 MHz and 108.48 MHz, respectively. The relative error between the analytical estimate and numerical simulation is <3% for $f \geqslant 27.12$ MHz.

The electron-coupling power is consumed by elastic collisions (P_{el}) and inelastic collisions (P_{inel}). P_{el} is used to supply energy to the momentum transfer of electrons with the molecules and atoms of the feedstock gas, for example

e + He → e + He and e + O$_2$ → e + O$_2$. Large P_{inel} is in general desirable because it is used for reactive species production. Figure 4 shows how the electron-coupling electrical power is partitioned onto elastic collisions, inelastic collisions, and ROS generation, as well as how this power partition is modulated by the driving frequency. The power density dissipated in elastic collisions increases with the driving frequency, whereas the dissipated power density in inelastic collisions increases slightly from 13.56 to 27.12 MHz before decreasing monotonically.

Among the inelastic collisions, the electron-impact reactions for O, O* and O$_2^*$ generation are of great interest. Figure 4(*b*) shows that $P_{\mathrm{O}_2^*}$ monotonically increases with frequency, while P_O and P_{O^*} share a similar dependence with P_{inel}. From $f = 13.56$ to 108.48 MHz, $P_{\mathrm{O}_2^*}$ increases by 43%, while P_O and P_{O^*} decrease by about 14%. Production of O$_2^*$ requires low electron energy (e.g. e + O$_2$ → O$_2(a\,^1\Delta_g)$ + e, 0.977 eV; e + O$_2$ → O$_2(b\,^1\textstyle\sum_g^+)$ + e, 1.627 eV), whereas production of and O (and O*) needs energetic electrons (e.g. e + O$_2$ → 2O + e, 5.58 eV; e + O$_2$ → O(^1D) + O + e, 8.6 eV). The very low-energy thresholds for the former are reached easily even in the plasma bulk region, suggesting O$_2^*$ generation mainly dependent on the electron density and largely uninfluenced by the sharp fall in the maximum electron temperature, $T_{e,\max}$ (in the sheath). The 43% increase in $P_{\mathrm{O}_2^*}$ is similar to the 36% increase in the space-averaged electron density in the 13.56–108.48 MHz range. By contrast, the production of O and O* is more sensitive to the large reduction in $T_{e,\max}$ with increasing frequency. From 13.56 to 27.12 MHz, $T_{e,\max}$ decreases by about 27% and the space averaged electron density increases by 36%. Their competition results in a very modest 1% increase in P_O and P_{O^*} from 13.56 to 27.12 MHz at which their peak values are reached. From 27.12 to 108.48 MHz, P_O and P_{O^*} undergo an identical monotonic decline of 15%, whereas the maximum electron temperature reduces by 26%, similar to its 27% fall in 13.56–27.12 MHz. However the comparatively large fall in P_O and P_{O^*} from 27.12 MHz upwards is most likely due to the drastically reduced maximum electron temperature (from 5.63

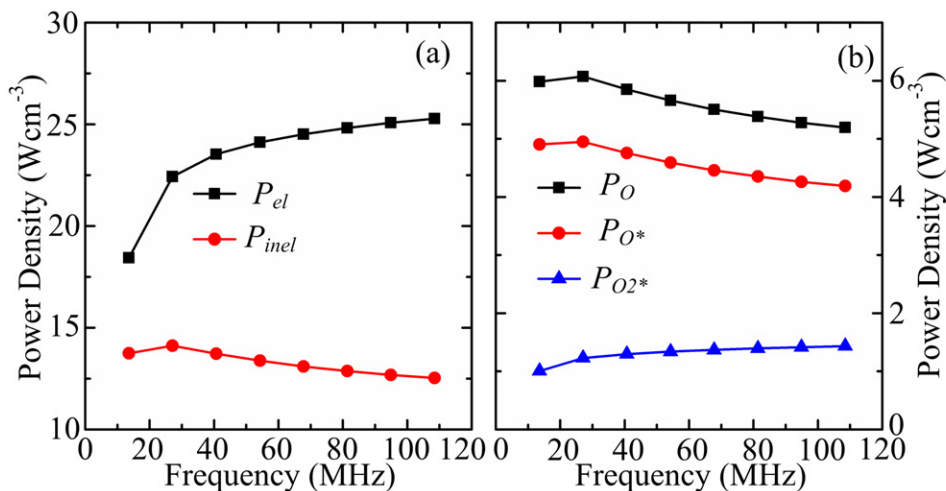J. Phys. D: Appl. Phys. **46** (2013) 415201

A Yang *et al*

Figure 4. Frequency dependence of time- and space-averaged power density in (*a*) elastic (P_{ei}) and inelastic collisions (P_{inel}); and (*b*) generation of O (P_O), O* (P_{O*}) and O_2^* ($P_{O_2^*}$).

to 4.16 eV), now below the energy thresholds for O and O* generation (8.6 and 5.58 eV).

To see the above discussions in a clear reference of electron-heating parameters (i.e. T_e, n_e), the frequency dependences of the electrical power density dissipated in electrons, inelastic collisions, and O, O* and O_2^* are summarized in table 1 with the power density symbols identical to those in figure 4. The 8-fold increase in frequency is seen to increase, desirably, power coupled to electrons but cause an overall reduction in power dissipation in inelastic collisions. The dissipated power density in inelastic collisions shares a similar trend of a small rise from f_0 to $2f_0$ and then a decay to $8f_0$ with P_O and P_{O*}. Reactions for generation of O and O* are associated with large threshold energies (5.58, 8.6 eV), and the resulting sensitive dependence of their production on $T_{e,max}$ is largely responsible for the monotonic decay of P_O and P_{O*} at $f \geqslant 27.12$ MHz. By contrast, the energy threshold for O_2^* generation is very low at 0.97 and 1.627 eV, thus allowing almost all electrons throughout the electrode gap to contribute to O_2^* generation. Consequently, the frequency dependence of $P_{O_2^*}$ follows that of the electron density, with the former undergoing an increase of 43% and the latter 45%. Therefore ROC sharing the power dissipation in inelastic collisions have distinctively different dependences on the driving frequency. No simple correlation of power dissipation in electrons and/or inelastic collisions to that in ROC may be drawn.

Together with previous studies of RF atmospheric-pressure helium plasmas, data in table 1 suggest that a small oxygen admixture does not affect the prevailing trend of increasing electron density and decreasing electron energy with frequency. For atomic oxygen in atmospheric He + O_2 plasmas, the energy thresholds for their generation are markedly above the space-averaged electron energy in the sheath region, thus leading to a sensitive dependence of their production on the electron temperature. By contrast, generation of excited oxygen molecules has a very low-energy threshold easily reached by most electrons and as a result the electron density dictates the frequency trend of

O_2^* generation. The contrast in the dependence on electron energy or density is therefore responsible for the different frequency dependence of oxygen atoms and excited oxygen molecules. The regulation of the chemical composition of reactive plasmas by the driving frequency is highly beneficial in terms of tailoring and control of plasma applications. The ability of regulating plasma chemistry is equally desirable for mechanistic studies as key factors responsible for plasma efficacy can be contrasted out from each other. This and other conclusions drawn from the above discussion are likely to be applicable beyond the atmospheric He + O_2 plasma studied here, because the main mechanisms for O, O* and O_2^* production are direct electron dissociation and direct electron excitation without participation of other gases in the feedstock gas (i.e. helium in the case of this study).

5. ROS generation mechanisms

Power dissipation in electrons and in electron-impacting generation of reactive plasma species shown in figure 4 are used to produce O, O* and O_2^* as well as other reactive species such as O_3 and O_2^-. The latter need to be studied in terms of their concentrations. Figure 5 illustrates the phase-averaged spatial distributions of four neutral ROC (i.e. O, O*, O_2^* and O_3) at different driving frequencies. In terms of time- and space-averaged concentrations, the ground state O is the dominant neutral ROS followed by O_2^* and O_3 in that order. These three species have their densities between 10^{15} and 10^{16} cm^{-3}. The excited-state oxygen atom O*, mainly O(1D) and O(1S), has an averaged density of $(1.5–1.8) \times 10^{12}$ cm^{-3}, some three orders of magnitude lower than the other three ROS. With the driving frequency increased from 13.56 to 108.48 MHz, the time- and space-averaged density of O_2^* increases by about 44% and the density of O_3 decreases by about 74%. The ground state and excited oxygen atoms, on the other hand, are seen to experience a much smaller reduction of 4% and 3%, respectively, from 13.56 MHz to 108.48 MHz. The spatial profiles of the four neutral ROS vary differently with the driving frequency. With

Table 1. Trend of electron heating and power dissipation.

f (MHz)	d_s (μm)	$T_{e,max}$ (eV)	n_e (10^{10} cm^{-3})	Power density (W cm^{-3})				
				P_e	P_{inel}	P_O	P_{O^*}	$P_{O_2^*}$
13.56	527	7.71	1.08	32.3	13.7	6.00	4.90	0.99
27.12	308	5.63	1.37	36.6	14.1	6.07	4.95	1.22
54.24	181	4.17	1.46	37.5	13.4	5.66	4.60	1.34
108.48	124	4.16	1.47	37.8	12.5	5.19	4.19	1.43
Trend	↓	↓	↑	↑	↑↓	↑↓	↑↓	↑
x_{8f0}/x_{f0}	0.24	0.54	1.36	1.17				1.44
x_{8f0}/x_{2f0}					0.63	0.86	0.85	
Threshold energy of reaction (eV)						5.58	8.60	0.97

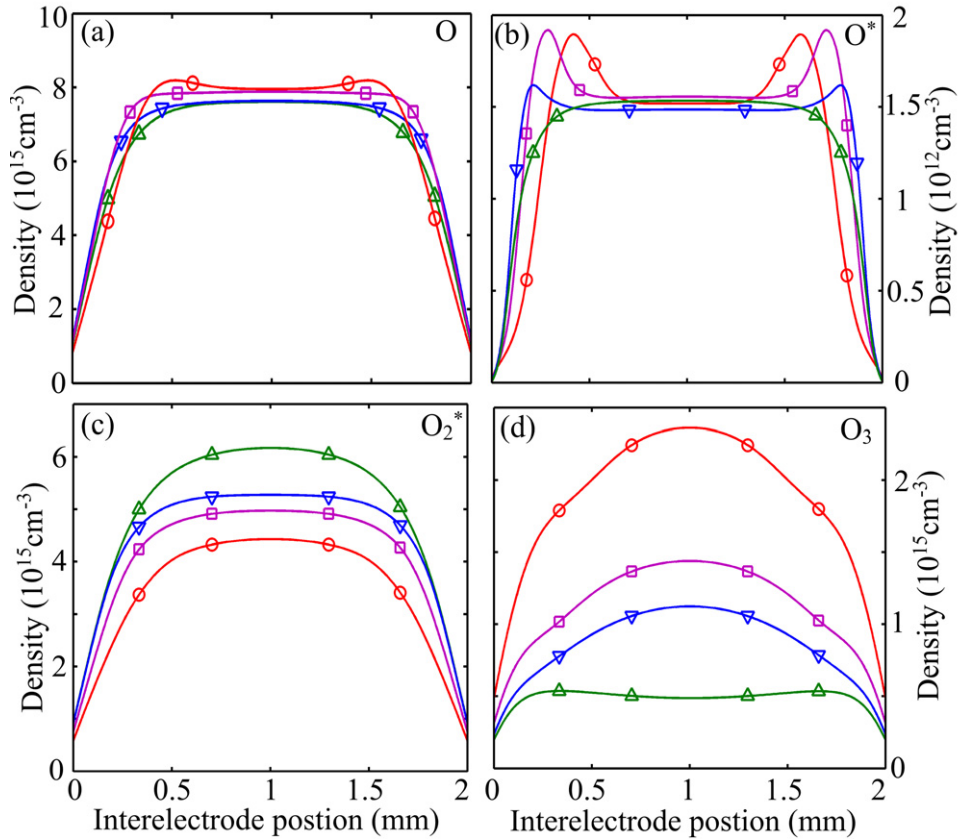*Note*: ↑: rise trend, ↓: fall trend, red arrow: dominant trend.

Figure 5. Spatial profiles of phase-averaged neutral ROS densities at 13.56 MHz (–○–), 27.12 MHz (–□–), 54.24 MHz (–▽–) and 108.48 MHz (–△–).

increasing frequency, the spatial profiles of O, O* and O$_2^*$ are seen to move towards the electrodes, whereas the O$_3$ profiles move away from the electrodes. The density profiles of O, O$_2^*$ and O$_3$ have a largely bell shape, whereas the O* profile has a predominately bimodal shape which changes to a bell shape at 108.48 MHz. The bimodal shape, as seen mostly clearly in the O profile at 13.54 MHz and the O* profile below 108.48 MHz, is indicative of a strong contribution of large electron energy in the sheath region. The transition to the bell shape represents a much-reduced contribution of sheath electrons that suffer drastic energy reduction at high frequencies. For O* whose generation has the highest threshold energy, the appearance of the bimodal profile and its transition to the bell shape is most distinctive. This is easily detectable experimentally via

a spatially resolved spectrum of its optical emission at 777 and 844 nm.

O, O* and O$_2^*$ are mainly produced by electron-impact reactions, and their production is sustained by the dissipated power densities in figure 4(*b*). Take O$_2^*$ for instance; its concentration increases by 44%, identical to the increase of 44% in its dissipated power from 13.54 to 108.48 MHz (table 1). For O and O*, the frequency trends of their concentrations are the same as that of P_O and P_{O^*}, hence a similar concentration-power correlation. Unlike O, O* and O$_2^*$ (all generated by electron-impact reactions), ozone is mainly generated by O + O$_2$ + He → O$_3$ + He, and destroyed through O$_2(b\,^1\sum_g^+)$ + O$_3$ → 2O$_2$ + O and O$_2(b\,^1\sum_g^+)$ + O$_3$ → O$_2(a\,^1\Delta_g)$ + O$_2$ + O. Its concentration is therefore dependent
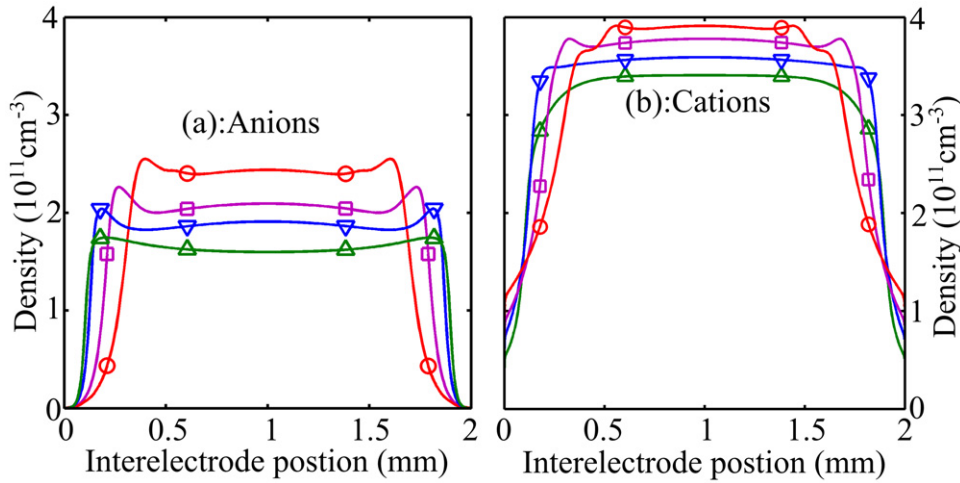
Figure 6. Spatial profiles of the phase-averaged (*a*) anion density and (*b*) cation density at 13.56 MHz (–○–), 27.12 MHz (–□–) 54.24 MHz (–▽–) and 108.48 MHz (–△–).

on O and O_2^*. With increasing frequency (i.e. $f_0 \to 8f_0$), the O_2^* density increases by 44% with an expanding profile towards the electrodes, whereas the O density reduces by 4%. These combine to result in a 74% reduction of the O_3 density with its profile receding from the electrodes. In other words, the frequency dependence of the O_3 concentration is largely controlled by its destruction route and hence by the frequency dependence of O_2^*. With increasing frequency, the O_3 concentration decreases due to an increase of the electron density. In practice, the O_3 reduction is likely to be more as the gas temperature is likely to be elevated at higher frequencies [15].

Charged particles are capable of promoting important effects on polymeric and biological materials. For example, electrons are directly involved in redox chemistry and can dynamically influence the ion channels of the cell membrane [50–52]. In addition, superoxide (O_2^-) is a biologically important oxidant [43]. Figure 6 shows the spatial profiles of the phase-averaged densities of charged species at different driving frequencies. It is seen that both anions and cations are confined in the centre region by the ambipolar field [33] and with increasing frequency their density profiles broaden due to the decreasing thickness of the sheath region. Anion and cation densities decrease with increasing frequency, and as their profiles broaden the peak anion density decreases by 25% and the peak cation density decreases by 6%.The space-averaged anion and cation densities undergo smaller reduction. These are consistent with an electronegativity reduction of $\alpha = 1.64 \to 1.01$.

The main anions are O^- and O_3^-, whereas O_2^+ is the dominant cation. Generation of O^- is mainly through $e+O_2 \to O^- + O (4.12\,eV)$ and $e+O_3 \to O^- + O_2 (3.54\,eV)$. Their modest threshold energies mean that the increase in n_e and the decrease in T_e with frequency have little effect on the contribution of electrons, for example the reaction rate of the former is found to remain little changed (data not shown). However the 74% reduction in n_{O_3} (see table 2) decreases the O^- production via the latter reaction, leading to an overall reduction in the O^- concentration. For O_3^- whose generation is mainly through

$O^- + O_2 + M \to O_3^- + M$, the O^- trend suggests a decreasing frequency dependence of the O_3^- density. As a result, the total anion density decreases with increasing frequency, as indicated in figure 6(*a*).

It is of interest to consider O_2^- due to its direct relevance to biology [43]. In the RF atmospheric He + O_2 plasma, O_2^- is produced mainly through $O_3^- + O \to O_2^- + O_2$ without directly involving electrons (hence, no threshold energy). Its reaction rate is affected by the decreasing frequency dependence of O_3^- and the increasing frequency dependence of O (to 27.24 MHz) (figure 6(*a*) and table 2). Overall, the change in the O_2^- concentration remains within 6%. For cations on the other hand, the generation of O_2^+ is mainly through electron-impact ionization ($e+O_2 \to O_2^+ + 2e$), the rate of which decreases with increasing frequency (shown in figure 2(*c*)). This suggests decreasing frequency dependence for the cation density as shown in figure 6(*b*). Table 2 summarizes the frequency dependences of densities of main neutral and charged plasma species.

As already mentioned, the contrasting frequency trends of different plasma species are a valuable route of modulating plasma chemistry especially when through one single electrical parameter (i.e. the driving frequency). In the context of plasma biosciences, this offers a hitherto little suggested strategy of tuning up and down different oxidation stresses. For example, many human diseases are linked to an inappropriate balance of different ROC (e.g. nitric oxide and superoxide) [53, 54]. Table 2 indicates that an increase in the driving frequency reduces the participation of O_3 and O_2^- and increases that of O_2^*. This suggests a simple and effective way to modulate relative concentrations of different reactive species and hence their balance in the plasma. In turn, the modulation in plasma ROS composition could be used to address possible *in vivo* ROS imbalance specifically to individual patients. It is worth noting that an alternative route of modulating the balance of plasma ROS is modification to the chemical composition of the feedstock gas [55]. So there is considerable scope to manipulate plasma chemistry for specific applications.

Table 2. Averaged concentrations of key plasma species.

f (MHz)	$T_{e,max}$ (eV)	$n_e \times 10^{10}$	Particle concentration n (10^{15} cm^{-3})					
			n_O	$n_{O^*} \times 10^3$	$n_{O_2^*}$	n_{O_3}	$n_{O_2^-} \times 10^5$	$n_{O_2^+} \times 10^3$
13.56	7.71	1.08	6.70	1.31	3.48	1.88	3.29	2.63
27.12	5.63	1.37	6.90	1.42	4.12	1.13	3.51	2.66
54.24	4.17	1.46	6.68	1.36	4.49	0.86	3.64	2.59
108.48	4.16	1.47	6.45	1.27	5.01	0.49	3.48	2.40
Trent	↓	↑	↑↓	↑↓	↑	↓	↑↓	↓
x_{8f0}/x_{f0}	0.54	1.36	0.96	0.97	1.44	0.26	1.06	0.91
x_{8f0}/x_{2f0}			0.93	0.89			0.99	
Threshold (eV)			5.58	8.60	0.97	0.97	N/A	12.1

Note: ↑: rise trend, ↓: fall trend, red arrow: dominant trend.

6. Wall fluxes of reactive species

The high collisionality of atmospheric-pressure plasmas leads to a very short transport distance of almost all plasma species during their lifetime, typically shorter than the sheath thickness [42]. This is distinct from the case of low-pressure plasmas in that the dose of atmospheric-pressure plasmas as experienced by a sample placed on a plasma-facing wall (e.g. an electrode) is supplied from a boundary layer of up to a few hundreds μmin width next to the sample surface rather than from further away within the plasma bulk. The wall fluxes reaching the sample surface are therefore controlled locally by physics and chemistry within the micron-scale boundary layer [42]. In other words, the space-averaged densities are not the most appropriate indicator of plasma dose experienced by the sample.

To see how the electrode fluxes may change with the driving frequency, figure 7 shows spatiotemporally averaged densities and time-averaged electrode fluxes of neutral plasma species as a function of the driving frequency. Similar to their densities, the electrode flux of the ground state O is the largest followed by O_2^*, O_3 and O^* in that order with the O^* flux now four orders of magnitude below the wall fluxes of others. Clear difference and similarity in the frequency dependence are seen between concentrations and wall fluxes in figure 7. Take ground-state atomic oxygen as an example, its concentration and its wall flux share a very similar frequency dependence of an initial rise and then a large fall. However distinct differences do exist. For the O concentration, its initial increase is only about 3% and its subsequent fall is also small at 6% having its peak reached at 27.12 MHz. By contrast, the initial rise and subsequent fall of the O wall flux is much larger, at 41% and 13% respectively, and its maximum value occurs at a higher frequency of 54.24 MHz. Similarly for the excited atomic oxygen, the change in its density is much smaller (6%) than that in its wall flux (43%). Therefore, for applications in which the role of O/O* is dominant, high- frequency operation is in fact more desirable than the frequency dependence of their concentration may imply.

Of neutral oxygen molecules, the concentration and the wall flux of O_3 decrease monotonically with frequency, by 74% and 60%, respectively. On the other hand, O_2^* undergo marked increase in both their concentration (43%) and their wall flux (60%) from 13.56 to 108.48 MHz, although the decline of the

wall flux beyond 83 MHz is very slight. Compared to their respective concentrations, O_3 experiences a smaller change in its wall flux but O_2^* undergoes a larger change.

The contrast between concentration and wall flux has recently been attributed to the short lifetimes (τ) and short transport distance of plasma species at elevated gas pressure [42]. For plasma species with short lifetimes, they may not be able to reach a sample if the distance from the location of their generation to the sample surface is longer than the distance that they can transverse during their lifetime. For neutral species, the effective excursion distance during lifetime, i.e. EDL, may be estimated from the product of the thermal velocity of a neutral species k and its lifetime τk, or EDL $= v_{th,k}\tau_k$. This represents the thickness of a boundary layer above the sample surface, outside which plasma species generated are unable to reach the sample. The lifetimes of O, O_2^* and O_3 in plasma, are more than 1 ms, but for O^* it is less than 1 μs. For an atmospheric-pressure He + O_2 discharge at 13.56 MHz, it is found that the EDL of neutral species are $L_O = 285 \mu$m, $L_{O_2^*} = 284 \mu$m, $L_{O_3} = 223 \mu$m and $L_{O^*} = 6 \mu$m [33]. The EDL are little affected by change in the driving frequency, as they are dictated by destruction processes unrelated with electron density and electron temperature.

As the sheath thickness decreases with frequency (figure 1(*a*)), the boundary layer of a frequency-independent width changes from being a fraction of the sheath region to expanding into the plasma bulk. This is illustrated in table 3. The EDL selects electron energy and density specific to the boundary layer for generation of plasma species that can reach a sample and contribute to application efficacy. Take O as an example, its EDL is shorter than d_s at frequencies at or below 27.12 MHz and so the O production is less sensitively dependent on the variation of $T_{e,max}$ near the sheath boundary. This is an important factor for the larger initial increase in the O wall flux and its continuation to a higher frequency of 54.24 MHz. For O_2^* on the other hand, its concentration and its wall flux share a similar frequency dependence. This is because the energy threshold for its generation is very low (i.e. 0.977 eV, 1.627 eV) and may be sustained almost anywhere in the gas gap. Hence, variation on EDL/d_s makes little difference. Detailed analysis of how electron energy and density in the boundary layer may influence the generation and wall flux of neutral plasma species follow the same methodology as that for space-averaged species concentrations
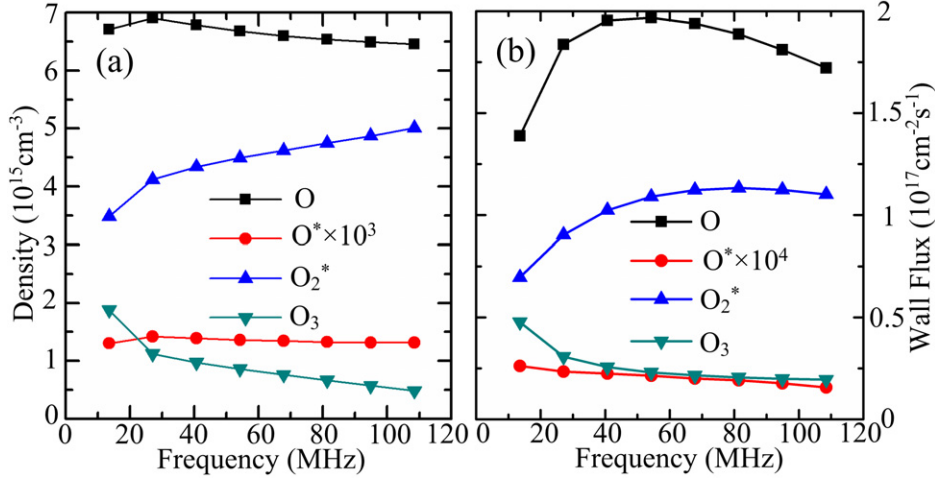
Figure 7. Frequency trends of (*a*) spatial-temporally averaged densities and (*b*) time-averaged wall fluxes of neutral ROS.

Table 3. Boundary layer width and ROS wall fluxes.

| f (MHz) | EDL/d_s | | DL/d_s | | Wall flux ratio $\Gamma(f)/\Gamma(f_0)$ | | | | | |
	O/O$_2^*$	O$_3$	e	O$_2^-$/10	O	O$_2^*$	O$_3$	e	O$_2^-$	O$_2^+$
13.56	0.54	0.4	1.2	0.18	1.0	1.0	1.0	1.0	1.0	1.0
27.12	0.93	0.7	1.0	0.11	1.3	1.3	0.6	0.5	0.1	0.47
54.24	1.57	1.2	0.8	0.09	1.4	1.6	0.5	0.2	0.03	0.22
108.48	2.30	1.8	0.6	0.06	1.2	1.6	0.4	0.1	0.01	0.09
Trent	↑	↑	↓	↓	↑↓	↑	↓	↓	↓	↓
x_{8f0}/x_{f0}	4.26	4.50	0.54	0.33	1.20	1.60	0.4	0.1	0.01	0.09
x_{4f0}/x_{f0}					1.40					
X_{8f0}/x_{4f0}					0.86					

Note: ↑: rise trend, ↓: fall trend, red arrow, dominant trend.
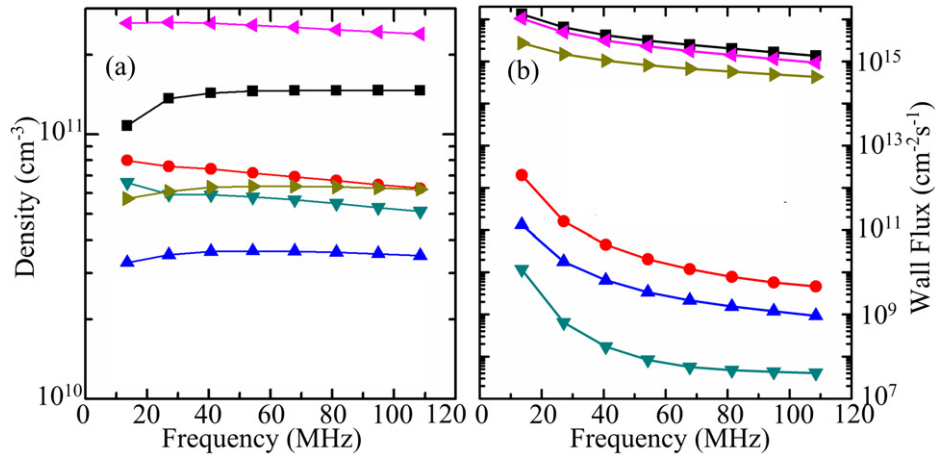

Figure 8. Spatial-temporally averaged densities (*a*) and temporal averaged electrode fluxes (*b*) of charged species. –■–:e, –●–: O$^-$, –▲–: O$_2^-$, –▼–: O$_3^-$, –◄–: O$_2^+$, –►–: O$_4^+$.

in section 5, and has been found to support observations of figure 7(*b*).

For charged species, figure 8 shows that the electrode fluxes of electron and cations are $\sim 10^{15}$ cm^{-2} s^{-1}, higher than that of anions by 4–7 orders of magnitude. As the driving frequency is increased from 13.56 to 108.48 MHz, the electrode fluxes of electron and cations decrease by ~ 1 order of magnitude while for anions they decrease by ~ 2 orders of magnitude. The decrease of the electron flux is due to the

enhancement of electron trapping with increasing frequency (see figures 1(*a*)–(*d*)). As shown in figure 1(*a*), the duration when the plasma bulk contacts an electrode is ~ 0.15 cycle at 13.56 MHz but its decreases rapidly to zero (i.e. no contact) when $f \geqslant 54.24$ MHz. To explain this, we define a drift length (DL) for charged species as

$$\text{DL} = \tfrac{1}{2} v_D T_{RF}, \qquad (5)$$

where v_D is the drift velocity and T_{RF} is the RF period. DL represents the distance that a charged species may travel

without changing direction (i.e. during one half RF) in the field of the electric field. The DL for electrons can be estimated by using a representative value of the electron mobility at $\mu_e = 1100\,\mathrm{cm^2\,V^{-1}\,s^{-1}}$ and the averaged electric field in the plasma bulk during one RF period.

Using equation (5), DL of electrons is found to be $608\,\mu\mathrm{m}$, $304\,\mu\mathrm{m}$, $152\,\mu\mathrm{m}$ and $76\,\mu\mathrm{m}$ for 13.56 MHz, 27.12 MHz, 54.24 MHz and 108.48 MHz, respectively. The DL may be also be used to explain frequency effects on the wall fluxes of cations. For simplicity, we assume an averaged cation mobility of $\mu_i = 20\,\mathrm{cm^2\,V^{-1}\,s^{-1}}$ for all the cations and that the cation wall fluxes persist for half a cycle. The latter allows for E to be estimated as the averaged electric field in the sheath over one half RF period. Numerical simulation suggests that the electric field in the sheath is strongly dependent on the driving frequency, and it decreases by about four times with increasing frequency from 13.56 to 108.48 MHz. With the RF period decreasing by a factor of 8 over the same frequency range, the DL of cations decreases by a factor of about 32 from 59 to $1.8\,\mu\mathrm{m}$. A smaller DL implies a weaker replenishment of relevant plasma species to compensate for their wall loss.

For anions, their fluxes are driven to the instantaneous anode by a rather weak electric field in the anode sheath. Assuming that electrode fluxes persist for one half RF cycle and using the space-averaged rms electric field to approximate the anode electric field, the drift distance is estimated to be $\mathrm{DL_{anion}} = 9\text{–}0.8\,\mu\mathrm{m}$, decreasing with increasing frequency from 13.56 to 108.48 MHz. Similar to cations, the smaller DL implies weaker replenishment, which is responsible for the decrease of anion fluxes.

From the above discussions, it is clear that the fluxes of neutral and charged species are controlled by physics and chemistry in their boundary layers immediately next to an electrode or a sample surface. For different plasma species, they have their own boundary layers of varying width from a few $\mu\mathrm{m}$ to a few hundreds of $\mu\mathrm{m}$. Difference in the boundary layer width originates from diffusion of neutral species and drift of charged particles, the former unaffected and the latter affected by the driving frequency. In addition, the numerical contrast in the boundary layer width selects spatial regions having very different frequency dependences of electron energy and electron density. As a result, production and wall fluxes of all plasma species becomes strongly influenced by the driving frequency.

ROC such as O/O^*, O_2^*, O_3 and O_2^- as well as electrons, cations and other anions are all capable of inducing strong effects on biological, polymeric and chemically contaminated materials. It is inevitable that specific characteristics of different applications make them more responsive to different reactive and charged plasma species. Persistent contaminants such as infectious proteins may be inactivated only with large dose of strong oxidants such as atomic oxygen, whereas *E. coli* inactivation could be readily achieved with ozone. Consideration of which ROS to use goes much beyond their oxidation potential, as a too strong oxidant can cause undesirable damage to healthy tissues. Figure 7(*b*) highlights contrasting frequency dependence of O/O^* and O_3 wall fluxes, and therefore it is both unrealistic and unhelpful to draw a

blanket conclusion on the choice of the driving frequency. Without being restricted by the specifics of applications, however, it is clear that an increase in the driving frequency leads to a sustained increase in the O_2^* flux (produced by electron excitation with low-energy thresholds of 0.977 eV and 1.627 eV), an increase in the O flux to about 55 MHz (by electron-impact dissociation), a monotonic decrease in the O_3 flux (lost through O_2^*), and also a monotonic decrease in the O_2^- flux (by electron attachment). The picture of contrasting frequency dependences offers a useful chart of trends of the individual ROS and the chemical composition of the ionized gas with which to cater for specific applications.

7. Concluding remarks

This contribution reports a detailed study of electron-heating mechanisms in RF atmospheric-pressure He + O_2 plasma and how the main electron-heating parameters (e.g. electron temperature and density) impact on the production of ROS in the sheath and the plasma bulk, as the driving frequency is increased eight-fold from 13.56 MHz. It has been shown that the frequency increase leads to a drastic fall in the peak electron temperature (by 46%) and a simultaneous increase in the space-averaged electron density (by 36%), accompanied by a considerable shrinkage of the sheath thickness (by 76%), a four-fold decrease in the sheath electric field, and much increased electron trapping. While the percentage changes may differ numerically from those found in comparable pure helium plasma with the same dissipation power density, the general trend holds true for electron temperature, electron density, sheath thickness, and electric field in the sheath as the driving frequency is varied. This is the prevailing plasma physics that drives all plasma reactions and underpins the generation of ROS.

With increasing frequency, a picture of contrasting evolution of key plasma parameters has been shown to emerge. Power dissipation in electrons increases monotonically, but that in inelastic collisions rises only briefly till 27.12 MHz before declining. Also, the trend of an initial rise followed by a fall has been found in the power dissipation in O and O^* as well as their space-averaged concentrations. For O_2^* by contrast, its dissipating power density, both its space-averaged concentration and its wall flux increase with frequency. Noting that production of O, O^* and O_2^* is predominantly through electrons, their contrasting frequency dependence has been attributed to the distinct difference in the threshold electron energies for their generation. Essentially plasma species generated mostly by energetic electrons are more susceptible to the sharp fall in electron temperature. By contrast, electrons are not directly involved in ozone generation (mainly though $O + O_2 + He \rightarrow O_3 + He$) and ozone destruction ($O_2^* + O_3 \rightarrow 2O_2 + O$, $O_2^* + O_3 \rightarrow O_2^* + O_2 + O$). The large increase in O_2^* leads to a large fall of O_3 in terms of both space-averaged concentration and wall flux.

As already suggested recently [33, 42], plasma species capable of reaching a sample are confined in a micron-scale boundary layer immediately above the sample surface. The origin of the boundary layer is the very high collisionality
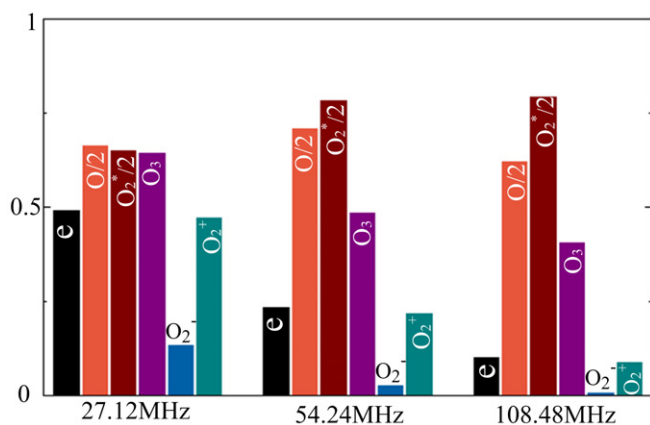
J. Phys. D: Appl. Phys. **46** (2013) 415201

A Yang *et al*

Figure 9. Wall fluxes of electrons, key charged and neutral plasma species at three high frequencies normalized to their individual values at 13.54 MHz.

of atmospheric-pressure plasmas that severely restricts the distance of particle diffusion and drift. This has been shown to introduce an additional complexity. As a result, the frequency dependences of wall fluxes of different ROS and charged species in the plasma are modified further, but retaining the character of contrasting dependences. Therefore distinct from the case of low-pressure plasmas, space-averaged particle concentrations are not the most appropriate indicator of what the sample may experience. A further point to note is that manipulation and regulation of plasma chemistry as experienced by the sample are locally achieved even though the control of such regulation (e.g. the driving frequency) may be introduced globally. Finally, the importance of local physics and chemistry adds the importance of surface conditions of the sample, for example chemicals released from the sample becoming involved in the boundary layer and possible evolution of surface conditions (e.g. secondary electron emission) with the time of plasma treatment. These are largely uncharted for low-temperature atmospheric-pressure plasmas [56]. It is of interest to comment on possible implications of the findings of this work on atmospheric plasmas not sustained between two parallel electrodes, for example atmospheric plasma jets and atmospheric plasma jet arrays [57–61]. It is anticipated that variation in the driving frequency may be used to effectively tune the production of long-living neutral species (e.g. O_3 and H_2O_2) and their delivery to a downstream sample. For charged species, the effectiveness of such control is likely to be influenced by how the plasma plume interacts with the downstream sample.

Differential regulation of the chemical composition of reactive plasmas by the driving frequency is highly beneficial in terms of tailoring and control for plasma applications. Figure 9 shows wall fluxes of electrons and key plasma species normalized to their respective values at $f_0 = 13.56$ MHz for $f = 2f_0$–$8f_0$. Plasma chemistry as manifested by the composition profile of different wall fluxes is clearly modulated by the driving frequency. The ability of regulating plasma chemistry may be used to contrast out the effects of different plasma species and indeed different flux composition profiles, desirable for both mechanistic and application studies. This work is an example of the importance of manipulating

electron-heating processes as a means to enabling controlled regulation of plasma chemistry, and for low-temperature atmospheric-pressure plasmas this is still a largely uncharted space.

Acknowledgments

References

[1] Hackam R and Akiyama H 2000 *IEEE Trans. Dielectr. Electr. Insul.* **7** 654
[2] Malik M A, Ghaffar A and Malik S A 2001 *Plasma Sources Sci. Technol.* **10** 82
[3] Lukes P, Appleton A T and Locke B R 2004 *IEEE Trans. Ind. Appl.* **40** 60
[4] Foster J, Sommers B S, Gucker S N, Isaiah M B and Grigory A 2012 *IEEE Trans. Plasma Sci.* **40** 1311
[5] Hu J and Gordon R G 1992 *J. Appl. Phys.* **72** 5381
[6] Sankaran R M, Holunga D, Flagan R C and Giapis K P 2005 *Nano Lett.* **5** 537
[7] Kong M G, Kroesen G, Morfill G, Nosenko T, Shimizu T, van Dijk J and Zimmermann J L 2009 *New J. Phys.* **11** 115012
[8] Fridman G, Shekhter A B, Vasilets V N, Friedman G, Gutsol A and Fridman A 2008 *Plasma Process. Polym.* **5** 503
[9] Suzuki T, Saburi T, Tokunami R, Murata H and Fujii Y 2006 *Thin Solid Films* **506–507** 342
[10] Arkhipenko V I, Kirillov A A, Simonchik L V and Zgirouski S M 2005 *Plasma Sources Sci. Technol.* **14** 757
[11] Wang X H, Yang A J, Rong M Z and Liu D X 2011 *Plasma Sci. Technol.* **13** 724
[12] Deng X T, Shi J J, Shama G and Kong M G 2005 *Appl. Phys. Lett.* **87** 153901
[13] Shi J J and Kong M G 2005 *J. Appl. Phys.* **97** 023306
[14] Lee M H, Park B J, Jin S C, Kim D, Han I, Kim J, Hyun S O, Chung K H and Park J C 2009 *New J. Phys.* **11** 115022
[15] Manley T C 1943 *Trans. Electrochem. Soc.* **84** 83
[16] Perni S, Shama G and Kong M G 2008 *J. Food Prot.* **71** 1619–25
[17] Perni S, Liu D W, Shama G and Kong M G 2008 *J. Food Prot.* **71** 302–8
[18] Fridman G, Peddinghaus M, Ayan H, Fridman A, Balasubramanian M, Gutsol A, Brooks A and Friedman G 2006 *Plasma Chem. Plasma Proc.* **26** 425
[19] Isbary G *et al* 2010 *Br. J. Dermatol.* **163** 78
[20] Park J, Henins I, Herrmann H W and Selwyn G S 2001 *J. Appl. Phys.* **89** 15
[21] Walsh J L, Zhang Y T, Iza F and Kong M G 2008 *Appl. Phys. Lett.* **93** 221505
[22] Shi J J and Kong M G 2005 *Appl. Phys. Lett.* **87** 201501
[23] Moon S Y, Kim D B, Gweon B and Choe W 2008 *Appl. Phys. Lett.* **93** 221506
[24] Liu D W, Iza F, Kong M G 2009 *Plasma Process. Polym.* **6** 446
[25] Radu I, Bartnikas R and Wertheimer M R 2003 *IEEE Trans. Plasma Sci.* **31** 1363
[26] Deng X T and Kong M G 2004 *IEEE Trans. Plasma Sci.* **32** 1709
[27] Xue J and Hopwood J A 2009 *IEEE Trans. Plasma Sci.* **37** 816
[28] Kogelschatz U, Eliasson B and Egli W 1999 *Pure Appl. Chem.* **71** 1819

[29] McKay K, Iza F and Kong M G 2010 *Eur. Phys. J.* D **60** 497
[30] Nosenko T, Shimizu T and Morfill G E 2009 *New J. Phys.* **11** 115013
[31] Liu D W, Iza F and Kong M G 2008 *IEEE Trans. Plasma Sci.* **36** 952
[32] Ellerweg D, Benedikt J, von Keudell A, Knake N and Schulz-von der Gathen V 2010 *New J. Phys.* **12** 013021
[33] Liu D X, Rong M Z, Wang X H, Iza F, Kong M G and Bruggeman P 2010 *Plasma Process. Polym.* **7** 846
[34] Waskoenig J, Niemi K, Knake N, Graham L M, Reuter S, Schulz-von der Gathen V and Gans T 2010 *Plasma Sources Sci. Technol.* **19** 045018
[35] Yang A J, Wang X H, Rong M Z, Liu D X, Iza F and Kong M G 2011 *Phys. Plasmas* **18** 113503
[36] Wang Q, Economou D J and Donnelly V M 2006 *J. Appl. Phys.* **100** 023301
[37] Sakiyama Y and Graves D B 2009 *Plasma Sources Sci. Technol.* **18** 025022
[38] Shi J J and Kong M G 2006 *Phys. Rev. Lett.* **96** 105009
[39] Iza F, Lee J K and Kong M G 2007 *Phys. Rev. Lett.* **99** 075004
[40] Deng X T, Shi J J and Kong M G 2007 *J. Appl. Phys.* **101** 074701
[41] Deng X, Shi J and Kong M G 2006 *IEEE Trans. Plasma Sci.* **34** 1310
[42] Liu D X, Yang A J, Wang X H, Rong M Z, Iza F, and Kong M G 2012 *J. Phys. D: Appl. Phys.* **45** 305205
[43] Halliwell B and Gutteridge J M C 2007 *Free Radicals in Biology and Medicine* 4th edn (Oxford: Clarendon)
[44] Bhoj A N and Kushner M J 2008 *Plasma Sources Sci. Technol.* **17** 035024
[45] Hagelaar G J M and Pitchford L C 2005 *Plasma Sources Sci. Technol.* **14** 722

[46] Liu D W, Shi J J and Kong M G 2007 *Appl. Phys. Lett.* **90** 041502
[47] Walsh J L, Iza F and Kong M G 2008 *Appl. Phys. Lett.* **93** 251502
[48] Monahan D D and Turner M M 2008 *Plasma Sources Sci. Technol.* **17** 045003
[49] Babaeva N Yu and Kushner M J 2010 *J. Phys. D: Appl. Phys.* **43** 185206
[50] Wang X H, Yang A J, Bai C F, Wang X Z, Liu D X, Rong M Z and Kong M G 2013 in preparation
[51] Finkel T 2011 *J. Cell Biol.* **194** 7
[52] Schoenbach K H, Joshi R P, Kolb J F, Chen N, Stacey M, Blackmore P F, Buescher E S and Beebe S J 2004 *Proc. IEEE* **92** 1122
[53] Darley-Usmar V, Wiseman H and Halliwell B 1995 *FEBS Lett.* **369** 131
[54] Beckman J S and Koppenol W H 1996 *Am. J. Physiol. Cell Physiol.* **271** C1424
[55] Walsh J L, Liu D X, Iza F, Rong M Z and Kong M G 2010 *J. Phys. D: Appl. Phys.* **43** 032001
[56] Oehrlein G S, Phaneuf R J and Graves D B 2011 *J. Vac. Sci. Technol.* B **29** 010801
[57] Stoffels E, Flikweert A J, Stoffels W W and Kroesen G M W 2002 *Plasma Sources Sci. Technol.* **11** 383
[58] Walsh J L, Shi J J and Kong M G 2006 *Appl. Phys. Lett.* **88** 171501
[59] Shashurin A, Keidar M, Bronnikov S, Jurjus R A and Stepp M A 2008 *Appl. Phys. Lett.* **93** 181501
[60] Cao Z, Nie Q, Bayliss D L, Walsh J L, Ren C S, Wang D Z and Kong M G 2010 *Plasma Sources Sci. Technol.* **19** 025003
[61] Kim J Y, Ballato J and Kim S O 2012 *Plasma Process. Polym.* **9** 253